PHYSICAL REVIEW B VOLUME 25, NUMBER 6 15 MARCH 1982

Structural characterization of ion-implanted graphite

B. S. Elman
Department of Physics and Center for Materials Science and Engineering, Massachusetts Institute of Technology, Cambridge, Massachusetts 02139

M. Shayegan and M. S. Dresselhaus
Department of Electrical Engineering and Computer Science and Center for Materials Science and Engineering, Massachusetts Institute of Technology, Cambridge, Massachusetts 02139

H. Mazurek*
Center for Materials Science and Engineering, Massachusetts Institute of Technology, Cambridge, Massachusetts 02139

G. Dresselhaus
Francis Bitter National Magnet Laboratory, Massachusetts Institute of Technology, Cambridge, Massachusetts 02139
(Received 9 November 1981)

Ion implantation of graphite is characterized with respect to lattice damage and the distribution of implanted ions. Both the depth profile of the damage and of the implanted ions are shown to follow the models previously developed for ion-implanted semiconductors. Raman spectroscopy is used in a variety of ways to monitor different aspects of the lattice damage while Auger spectroscopy is used to monitor the implantation profile. Both first- and second-order Raman spectra are reported as a function of ionic mass and ion energy. The surface damage is examined by scanning electron microscopy while the microcrystalline regions in an amorphous background are observed by scanning transmission electron microscopy.

I. INTRODUCTION

Ion implantation is a physical mechanism for the introduction of foreign species into host materials. Though widely studied in the case of semiconductors, this technique has only recently been applied to metals and semimetals. The applications to semiconductors have focused primarily on making devices by implanting either n- or p-type impurities.[1] The lattice damage which is associated with implantation is usually annealed out and the resulting material is further processed to make devices. The implantation of metals and semimetals has recently been undertaken[2–5] in an attempt to modify surface electronic structure to stimulate catalytic activity or to retard corrosion. The present study on implanted graphite was undertaken because of the known ability to chemically dope graphite to form intercalation compounds and make large changes in the electrical properties.[6]

Upon ion implantation, the distribution of ion impurities in amorphous target materials is a Gaussian function of distance into the sample and is characterized by the penetration depth R_p and spread of ions ΔR_p. These parameters of the implantation process can be calculated to a good approximation using the Lindhardt, Scharff, and Schiott (LSS) theory[7] and ion stopping-power tables.[8] Both the implantation parameters and the stopping power are dependent on many variables in a complicated but predictable way. A major objective of the present work is to test whether this theory, generally used for noncrystalline targets, is applicable to the implantation of ions into graphite, a crystalline material.

Some of the advantages of ion implantation over chemical means for the introduction of impurities into host lattices are that it is possible to implant almost any atom of the periodic table or even fragments of molecules. For example, with ion implantation it is possible to introduce chemical species that cannot be chemically intercalated. Also, by continuous change of the energy of implantation it is possible to obtain a large variety of

 ©1982 The American Physical Society

impurity distributions. In contrast to the diffusion process where the surface concentration and distribution of impurities are determined by the temperature, in the case of ion implantation, these two parameters can be varied independently. The doping profile is determined by the accelerating voltage, while the concentration is determined by the fluence of implantation. In contrast to the process of diffusion, implantation can be carried out over a wide temperature range. Moreover, the concentration of impurities is not limited by the solubility of the host materials. Because of the high kinetic energy of insertion, it may be possible to create more stable materials with lower affinities for desorption of the guest species.

In the case of crystalline targets [highly oriented pyrolytic graphite (HOPG) for example], the processes associated with ion implantation have some additional features.[1] If the energetic ions enter the crystal along low-index directions, they can penetrate far into the sample by "channeling" between atomic planes, with significantly lower energy loss both via nuclear and electronic processes than would occur in noncrystalline targets. When ion channeling occurs, the impurity distribution becomes long range and non-Gaussian.[1] Only those ions which get scattered out of a channel by a lattice imperfection get implanted in the sample. The occurrence of channeling depends also on the surface of the target and the amplitude of the thermal vibrations. The channeling effect, studied predominantly in germanium and silicon,[1,9] is found to fall off rapidly with angle away from the low-index channeling directions (axes or planes). Since graphite is a crystalline target, depth-profile studies by Auger-electron spectroscopy (AES) have been used to investigate whether the channeling effect occurs in graphite targets. The results provide strong evidence that for our experimental conditions no channeling effects are observed when implanting c faces of graphite. This is one of the major findings of the present work.

One of the disadvantages of ion implantation is that at heavy fluences (if the concentration of impurity is higher than a few at. %), lattice damage and intense lattice strains develop, leading to surface damage of the target. This surface damage, reported here for the first time for ion-implanted graphite samples, is studied by scanning electron microscopy (SEM) as a function of ion fluence and species.

The high kinetic energy of the implanted ions introduces lattice disorder and radiation damage which affect various physical properties of the host materials. In this context, ion implantation provides a technique for artificially producing disordered regions of varying thicknesses and at varying distances from the surface by appropriate selection of the fluences, accelerating voltage and ion species. This allows us to study the evolution of the microscopic structural properties of a very important sequence of regimes: crystalline-microcrystalline-amorphous.[5] Also of interest and importance is our ability to follow these regimes in reverse order by use of the annealing technique.

In addition to SEM studies of the surface damage and depth-profile studies by AES, this paper focuses on the presentation of new Raman scattering results on ion-implanted graphite. Raman scattering has already been widely exploited to characterize ion-implanted Si (Refs. 2–4, and 10–12) and graphite (Refs. 3, 5, and 13–15). In silicon, the method was used as a tool for local characterization of the crystalline quality of laser-annealed layers,[16,17] for observation of the amorphous-to-crystalline transition,[18] and for monitoring the introduction of disorder within the implanted layers. The view that the disordered region in silicon becomes amorphous up to the surface for high-ion fluences is supported by the observation of similar optical-absorption,[2,19] electron-paramagnetic-resonance[2,20] (EPR), and Raman scattering[2,21] results in silicon implanted at high ion fluences and in amorphous thin Si films made by evaporation or sputtering. Raman scattering has also been used to determine conductivity changes in semiconductors, where the plasma frequency has been varied by ion implantation,[22] to study local modes associated with the implanted species,[23–25] and to monitor ion implantation into diamond.[26–28]

The Raman and ir reflectivity spectra of HOPG have been measured and all symmetry-allowed active modes have been observed.[29] It is well known[5,30–33] that the Raman spectrum of microcrystalline forms of graphite shows additional disorder-induced lines (not observed in HOPG or single-crystal graphite) at ~ 1360 cm^{-1} in the first-order spectrum and at ~ 2970 cm^{-1} in the second-order spectrum. These disorder-induced lines correspond to a strong maximum in the phonon density of states at ~ 1360 cm^{-1} and to a combination $(1620+1360)$ cm^{-1}$=2980$ cm^{-1} of two maxima in the density of phonon states.[5,31,32,34] It was found that the relative intensity of the ~ 1360-cm^{-1} line with respect to the

$\sim$1580-cm^{-1} Raman-active E_{2g2} mode varies as the inverse of the crystal planar domain size, L_a.[33] This result is generally used to determine L_a from the Raman spectra. Results for thin (<2500 Å) amorphous carbon films deposited on glass substrates show one very broad asymmetric Raman line in the first-order spectra,[35] while for thick carbon films deposited on graphite and aluminum substrates,[36] the Raman spectra show two resolved features[35–37] peaking near 1580 and 1360 cm^{-1}.

Previous Raman studies on ion-implanted[3,4,14] and neutron-irradiated[15] graphite have been summarized elsewhere,[5] including results for the first- and second-order Raman spectra from ^{11}B-implanted graphite, and the effect of annealing. Previous work shows that the second-order spectra are even more sensitive than the first-order spectra for monitoring the threshold for the formation of heavy lattice damage within the optical skin depth. As the ^{11}B ion fluence increases above 1.0×10^{15} ions/cm^2, the implanted graphite samples lose their sharp second-order Raman spectra and simultaneously develop a Breit-Wigner line shape in their first-order spectra.[5,38] The striking similarity of the first- and second-order Raman spectra in heavily ion-implanted graphite to the spectra found in stage-1 alkali-metal donor compounds strongly supports a disorder-induced phonon mechanism for the origin of the broad continuum which gives rise to the Breit-Wigner line shape.

In the present study, attention is focused on the ionic mass and energy dependence of the amount of disorder introduced during the ion-implantation process. Results for the linewidth of the $\sim$1360-cm^{-1} disorder-induced line versus ionic mass at different fluences show that the dramatic increase in the linewidth of this line can be correlated with the appearance of a highly disordered region within the optical skin depth.[36] The effect of high-temperature annealing (in an argon atmosphere) on the line shape of the Raman-allowed $\sim$1580-cm^{-1} line was investigated, and our results show that the temperature where the Raman-allowed line becomes Lorentzian corresponds to the temperature of the second step of graphitization of various carbons. This temperature is well known from x-ray and diamagnetic susceptibility measurements of different forms of carbons,[36,39] and corresponds to the onset of three-dimensional ordering.

II. EXPERIMENTAL DETAILS

Samples of HOPG have been implanted with carbon ^{12}C and ions of atomic mass less (^{4}He, ^{6}Li, ^{9}Be, ^{11}B) and greater (^{19}F, ^{27}Al, ^{31}P, ^{75}As) than that of carbon. The implantation was done by directing an ion beam from an ion implanter (Accelerators Inc. 300R) normal to the *c* face of the samples.[5] For the Raman measurements the implantation was performed at ambient temperatures with fluences in the range $1.0\times10^{14}\leq\phi\leq1.0\times10^{16}$ ions/cm^2 and at an energy of 100 keV. The dependence of the Raman spectra on energy was studied using ^{4}He-ion-implanted samples at a fluence of 1.0×10^{15} ions/cm^2 and with energies in the range $40\leq E\leq200$ keV. Six high-fluence samples were specially prepared for AES studies, and the sample characteristics (ion species, fluence, and energy) are given in Table I. High fluences were needed to make quantitative Auger measurements.

Surface mechanical damage due to the implantation process was monitored by a Cambridge Mark

TABLE I. Characteristics of the ion-implanted samples used for Auger studies.

Ion species	Energy (keV)	Fluence (10^{17} ions/cm^2)	Calculated[a] R_p (Å)	Calculated[a] ΔR_p (Å)
^{11}B	75	1.00	2194	445
^{11}B	100	1.00	2817	502
^{11}B	125	1.00	3390	544
^{11}B	100	2.50	2817	502
^{31}P	100	1.00	979	292
^{75}As	100	0.326	486	128

[a]Values for R_p and ΔR_p calculated from LSS theory (Ref. 7) and electronic stopping-power tables (Ref. 8).

II Stereoscan scanning electron microscope (SEM) with a nondispersive x-ray attachment (KEVEX unit). Thin sections (<2000 Å), suitable for scanning transmission electron microscopy (STEM), were prepared from an ^{75}As-ion-implanted sample with $\phi=1.0\times10^{15}$ ions/cm^2 and $E=100$ keV, and STEM studies were made using a VG-HB5 STEM with *in situ* x-ray fluorescence (energy-dispersive) capabilities.

Auger electron spectra were obtained using a Physical Electronics Model 590A Scanning Auger Microprobe with argon-ion-sputtering capabilities. Depth profiles were obtained in high dosage ^{11}B-, ^{31}P-, and ^{75}As-ion-implanted samples by sputtering away the implanted surface and monitoring the Auger peak-to-peak intensities of the implanted elements as well as that of carbon. The relevant Auger transitions monitored were: the carbon 272-eV (*KLL*), boron 179-eV (*KLL*), phosphorous 120-eV (*LMM*), and the arsenic 1228-eV (*LMM*) transitions.

The Raman scattering experiments were performed at room temperature using a Brewster angle backscattering geometry. Incident radiation of 4880 Å and ~200 mW was provided by a cw argon-ion laser. The scattered radiation was collected at 90° to the sample surface, analyzed by a double-grating monochromator and detected by a cooled photomultiplier tube.[5]

The high-fluence ion-implanted samples were annealed in an argon atmosphere in the temperature range $900<T<2700$ °C to study the changes in the line shape of the first-order Raman-allowed line with the annealing temperature. The samples were found to be stable with respect to time and ambient laboratory atmosphere. No laser-annealing effects were expected or observed.

III. RESULTS AND DISCUSSION

We show in this work that the results of ion implantation into graphite can be well understood using models developed for semiconductor implants. For example, the dependence of the implantation profile on ion mass and energy is shown to fit quantitatively the theory of Lindhard, Scharff, and Schiott[7] (hereafter called the LSS theory), developed for amorphous semiconductors. The theoretical ion-penetration depth R_p, calculated by the LSS theory from electronic stopping-power tables,[8] is dependent on ion mass and energy, and the density of the host. According to this model, the depth profile is Gaussian in shape and is characterized by a linewidth ΔR_p [half-width at half-maximum (HWHM)]. Some pertinent values for R_p and ΔR_p are listed in Table II. Information on the depth profile of the implanted species is needed to interpret the Raman scattering results described below.

Graphite presents some very special implantation features associated with the layered nature of the host lattice. Because of the strong intralayer and weak interlayer bonding and the small (1.42 Å) nearest-neighbor in-plane distances, channeling is expected to occur only for *a*-face implantation. On this basis it is reasonable to expect that the LSS theory, originally developed for noncrystalline semiconductors, would apply to *c*-face ion implantation into graphite.

AES measurements were performed on the six high-fluence samples of Table I in an attempt to obtain depth profiles and compare the relative experimental parameters R_p and ΔR_p with theoretical values calculated from the LSS model. The Auger spectra were taken as the sample surface was sputtered away by argon ions to provide information on the ion concentration versus distance from the surface. The spectra obtained from all samples showed no Auger lines for the implanted species before sputtering the implanted surface. During the sputtering, the intensities of the 179-, 120-, and 1228-eV Auger lines for the ^{11}B, ^{31}P, and ^{75}As impurities, respectively, were measured as well as the 272-eV line for carbon itself. The sputtering profiles (Fig. 1) show Gaussian profiles for the impurities, thus having the line shape predicted by the LSS model. The intensity of the carbon line in Fig. 1 follows a Gaussian profile for

TABLE II. Values for R_p and ΔR_p for various ions implanted in graphite at 100 keV, calculated from the LSS theory (see text and Ref. 7) and electronic stopping-power tables (Ref. 8).

Ion	R_p (Å)	ΔR_p (Å)
^{1}H	9208	785
^{4}He	5946	698
^{9}Be	3460	551
^{11}B	2817	502
^{12}C	2379	463
^{19}F	1647	411
^{27}Al	1140	331
^{31}P	979	292
^{75}As	486	128

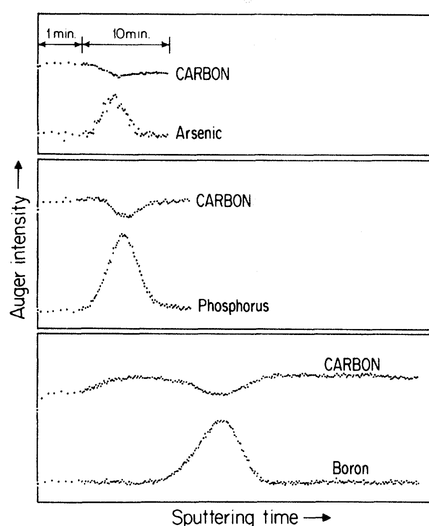

FIG. 1. Auger depth profiles of ^{11}B-, ^{31}P-, and ^{75}As-implanted graphite samples. The characterization of the samples is given in Table I. For each sample the peak-to-peak intensity of the carbon Auger line (272 eV), and that for the implant (using the Auger lines 179 eV for ^{11}B, 120 eV for ^{31}P, and 1228 eV for ^{75}As) are measured as a function of the sputtering time. See text for the discussion relating the sputtering time to the depth into the sample.

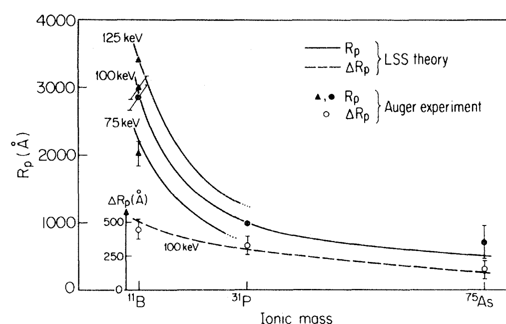

FIG. 2. Dependence on ionic mass and implantation energy of the penetration depth R_p and the implantation linewidth ΔR_p (HWHM). The points are determined from the Auger measurements (see text) and the curves are from the LSS theory.

carbon depletion in the same region as the impurity profiles peak.

To relate the sputtering profiles in Fig. 1 to the depth profiles, we note that the x axis is expressed in terms of the sputtering time. Since the sputtering rate (Å/min) for graphite was not known, no direct measurement of R_p could be made. In an attempt to quantify the AES depth profiles, we set the theoretical and experimental R_p values for the ^{31}P sample in Fig. 1 equal to each other, thus obtaining a calibration factor for converting sputtering time to distance (in Å). Using this calibration factor we determine experimental values for R_p for the different samples studied, assuming for simplicity that the sputtering rate for the samples is independent of the implanted-ion species. Good agreement between the results for R_p from this analysis (points) and the LSS theory (curves) is shown in Fig. 2, thereby establishing the validity of the LSS model for ion implantation into c faces of graphite.

Experimental values for ΔR_p are found as follows. We assume that the R_p distances in Fig. 1 match those predicted by the LSS model exactly. We thus obtain sputtering rates for each sample, from which we find the experimental ΔR_p values shown as open circles in Fig. 2. As this figure shows, the experimental ΔR_p dependence on ionic mass agrees well with the LSS theoretical values for ΔR_p.

The sputtering rates are found to be somewhat different (by a few percent) from one sample to another, which can be explained by the different binding energies for the various impurity ions, different degrees of disorder in the layers that were sputtered, experimental inaccuracies in the measurements themselves, and small departures of the experimental data from the LSS theory. From a calibration run performed on a Ta_2O_5 "standard" sample, we estimate the sputtering rate for ion-implanted graphite to be close to half of that for the Ta_2O_5 sample. This estimate will be helpful for future depth-profile studies of implanted graphite.

The depth profiles obtained from the ion-implanted graphite samples indicate that no perceptible surface sputtering occurred during the ion-implantation procedure. Also, ion implantation normal to the basal plane shows no evidence for channeling.

The intensity of the observed Auger signals (Fig. 1), along with the relevant sensitivity factors for different elements (available in the manual for the Auger instrument), can be used to obtain estimates of the composition of the implant and of carbon in the implanted region. For the ^{11}B ($\phi=2.5\times10^{17}$ ions/cm^2), ^{31}P ($\phi=1.0\times10^{17}$ ions/cm^2), and ^{75}As ($\phi=3.26\times10^{16}$ ions/cm^2) samples all implanted at $E=100$ keV, we obtain $C_{5.0}B$, $C_{16.0}P$, and $C_{8.4}As$ for the stoichiometries at R_p (maximum-implant density). The impurity concentrations are thus comparable to a close-packed arrangement of the impurity in its parent solid.

The Raman spectra are sensitive not only to the

impurities introduced by ion implantation, but also to the lattice damage that is produced within the optical skin depth. Thus the Raman spectra are also highly sensitive to the lattice damage in the region between the surface and $R_p - \Delta R_p$ (see Fig. 3). To characterize the ion-implanted samples with regard to lattice damage, SEM and STEM studies were carried out.

In the SEM studies it was found that for high-mass ions, even low-fluence implants cause sufficient disorder in the graphite crystal lattice to result in surface damage. This is illustrated by the SEM micrograph [Fig. 4(b)] for the ^{75}As-ion-implanted sample ($\phi = 1.0 \times 10^{15}$ ions/cm^2, $E = 100$ keV), which shows an extended "ridge" network on the entire surface. This result is in contrast with that for low ionic-mass implants (e.g., ^{11}B and ^{31}P) at identical fluences and energies, which exhibit surface micrographs indistinguishable from that of pristine HOPG; a SEM micrograph taken on HOPG at the same magnification ($\times 8000$) is shown in Fig. 4(a). To confirm that the samples studied by SEM had been uniformly implanted, x-ray fluorescence measurements were made with the SEM from different parts of the ^{31}P- and ^{75}As-ion-implanted samples. The results did confirm this.

The introduction of ions into graphite introduces strain into the host lattice, with larger strains and defect formation introduced by larger ions and higher fluences. Since the lattice damage of an ion increases as it is slowed down, the lattice damage increases as the implanted region is approached (see Fig. 3). As the ion mass increases, $R_p - \Delta R_p$ decreases so that the lattice-damaged region moves closer to the surface. We describe the highly damaged graphite region by a length R_s (see Fig. 3) measured from $R_p - \Delta R_p$, so that when R_s extends all the way to the surface (i.e., $R_s = R_p - \Delta R_p$), then significant surface damage is observed by SEM. Figure 4(b) shows a ridge structure identified with the onset of surface damage and attributed to the relief of lattice strain by surface buckling. The absence of ridge structures for SEM micrographs on ^{11}B- and ^{31}P-implanted samples at the same energy and fluence is attributed to $R_s < R_p - \Delta R_p$ so that for low fluences the R_s interface MM' is far from the surface and surface buckling does not occur.

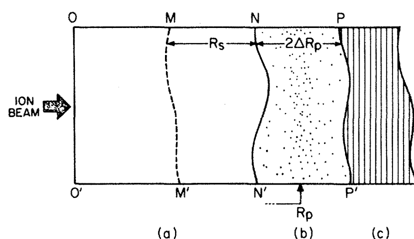

FIG. 3. Schematic view of the cross section of an ion-implanted sample of HOPG. The characteristics of regions (a), (b), and (c) are discussed in the text.

Considerable surface damage is found for implants in the high-fluence regime, independent of ionic mass. A SEM micrograph taken on a sample with a fluence of $\phi = 1.00 \times 10^{17}$ ^{31}P ions/cm^2 [Fig. 4(c)] shows that the ridges of Fig. 4(b) have "split open" forming "mesa and canyon" regions. The walls separating the mesas and canyons are planar sheets of graphite. The same kind of behavior was also observed for ^{11}B-ion-implanted samples. Thus, the implantation of ions with a penetration depth near 3000 Å may cause the surface to buckle

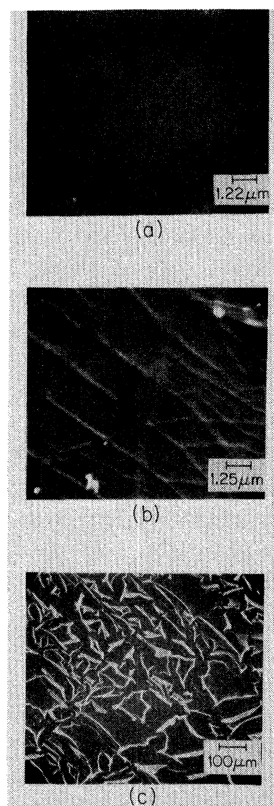

FIG. 4. (a) Scanning electron micrograph of pristine HOPG showing a smooth structureless surface. (b) Scanning electron micrograph of the ^{75}As-ion-implanted sample. The fluence was 1.0×10^{15} ions/cm^2 at 100 keV. (c) Scanning electron micrograph of the ^{31}P-ion-implanted sample. The fluence was 1.0×10^{17} ions/cm^2 at 100 keV. The micrograph shows extensive surface damage for implantation at this high fluence.

and split open if the ions are introduced with sufficient fluence. It is important to note, however, that from the LSS theory and our Auger studies, increasing the ion fluence only increases the concentration of the implanted ions at R_p, but does not alter R_p itself. The damage interface characterized by R_s (see Fig. 3), however, moves closer to the surface with increasing fluence, until finally a highly disordered region is formed extending from the surface to $R_p+\Delta R_p$ for sufficiently high fluences. Further information on R_s is obtained from the Raman measurements themselves, as discussed below.

STEM studies performed on a ^{75}As-ion-implanted sample ($\phi=1.0\times10^{15}$ ions/cm^2, $E=100$ keV) shows regions of both damaged and crystalline graphite (Fig. 5). Selected area diffraction patterns show that the darker areas in Fig. 5 are microcrystalline regions of ordered graphite, while the background is highly disordered. The average diameter of the dark regions is ~100 Å, while 5% of the surface is covered by the dark regions. This distribution is consistent with the Raman spectrum obtained for this sample which shows a broad disorder-induced line at ~1360 cm^{-1}. The crystal planar domain size L_a, calculated from our Raman spectra for the same sample as in Figs. 4(b) and 5 and using the calibration curve[33] of Raman intensities versus x-ray data, is ~94 Å, in excellent agreement with the STEM results.

The characterization discussed above allows us to consider any ion-implanted sample according to the model of Fig. 3 which delineates the following regions: (a) The region between lines OO' and NN' through which the ions pass but do not stop in appreciable concentrations. The region between MM' and NN', characterized by the length R_s, has considerable lattice damage, while the region between OO' and MM' is only partially disordered. (b) The region between lines NN' and PP' where the ions stop. The highly disordered region of the sample therefore lies between lines MM' and PP' and coincides with region (b) at relatively low fluences of implantation where $R_s\sim0$. (c) The region beyond PP' which remains essentially pristine graphite.

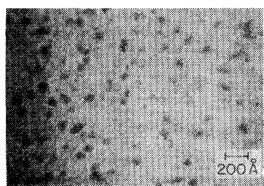

FIG. 5. STEM bright-field micrograph taken on a ^{75}As-ion-implanted sample with a fluence of 1.0×10^{15} ions/cm^2 at 100 keV. The dark areas correspond to crystalline regions (see text).

Another important parameter, which must be taken into account during the interpretation of the Raman spectra, is the penetration depth of light in disordered graphite δ. The parameter δ was measured experimentally by comparison between carbon films of different thicknesses deposited on graphite and aluminum substrates.[36] These measurements show[36] that δ is of order ~1000 Å for the laser line at $\lambda=4880$ Å, which is in good agreement with the calculated skin depth for HOPG, $\delta\simeq700$ Å.[40] Since we are able to observe the disorder-induced 1360-cm^{-1} line in the first-order Raman spectra[5] of ion-implanted samples, we expect to find a strong correlation between the broadening of the 1360-cm^{-1} line and the ratio R_p/δ. An advantage of studying the range of the disordered region introduced by ion implantation and the formation of a continuous amorphous region from the surface to $R_p+\Delta R_p$ is that by varying the ion species and keeping all other parameters the same, R_p and ΔR_p can be varied. The parameters R_p and ΔR_p can be calculated according to LSS theory and are given for several ions implanted at 100 keV in Table II.

It is clear that when δ becomes greater than $R_p-\Delta R_p-R_s$, the region between OO' and MM' in Fig. 3, then the Raman experiments become sensitive to the highly disordered region from MM' to PP'. From Table II we see that for low fluences of implantation (i.e., $R_s\rightarrow0$) the condition $\delta\sim R_p-\Delta R_p-R_s$ is then satisfied at the $\lambda=4880$-Å laser line, if we implant ions which are heavier than ^{27}Al. For ions of lower mass, much of the lattice-damage region extends beyond the optical skin depth, and therefore does not contribute to the Raman spectrum.

In Fig. 6 we present experimental data for the linewidth full-width at half-maximum (FWHM) of the disorder-induced 1360-cm^{-1} Raman line versus the ionic mass for different fluences, keeping the energy of implantation constant ($E=100$ keV). The figure shows that for fluences of $\phi=1.0\times10^{14}$ ions/cm^2, the onset of a rapid increase in the linewidth of the 1360-cm^{-1} line occurs for ionic masses $m>27$ (i.e., ^{27}Al ions). For fluences of $\phi=1.0\times10^{15}$ ions/cm^2, the onset occurs for $m>11$ (which corresponds to ^{11}B), and for $\phi=1.0\times10^{16}$ ions/cm^2, the onset occurs for $m>4$ (which corresponds to ^{4}He). The onset of the rapid increase in linewidth corresponds to satisfying the

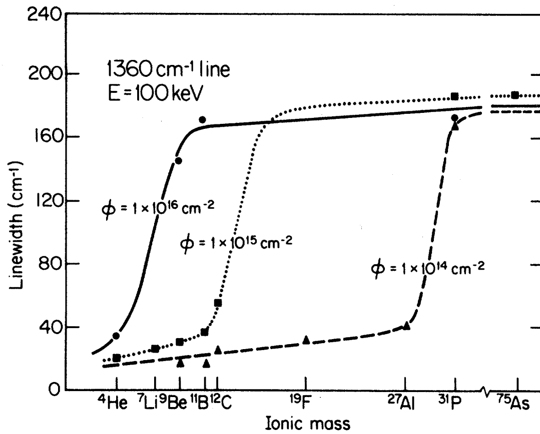

FIG. 6. Plot of the linewidth (FWHM) of the disorder-induced line at ~ 1360 cm^{-1} vs ionic mass for HOPG implanted with 100-keV ions at different fluences.

condition $\delta = R_p - \Delta R_p - R_s$. From Table II we note that $R_p - \Delta R_p$ for ^{27}Al is approximately equal to δ for the 4880-Å laser line. At the same time, Fig. 6 shows that for $\phi = 1\times 10^{14}$ ions/cm^2, the onset of the rapid increase in linewidth also occurs for the ^{27}Al ion, from which we conclude that $\phi \leq 1\times 10^{14}$ ions/cm^2 corresponds to the low-fluence regime ($R_s \cong 0$). It should be emphasized that after the broadening of the 1360-cm^{-1} line by an order of magnitude, the linewidth saturates at $\Delta_{1360} \simeq 180$ cm^{-1}, for all three fluences; the upper limit on Δ_{1360} corresponds to the width of the density-of-states peak.

This is in contrast with the linewidth of the Raman-allowed 1580-cm^{-1} line (Fig. 7), which saturates at different values of the linewidth for different fluences. In general, the behavior of the linewidth of the 1580-cm^{-1} line versus the ionic mass exhibits some similarities to that for the ~ 1360-cm^{-1} line with the main differences being: (1) for a given sample the linewidth of the 1580-cm^{-1} line is smaller than that for 1360-cm^{-1} line, (2) the linewidth at saturation is different for the various implantation fluences, and (3) the linewidth increases more gradually as a function of ionic mass.

For low fluence ($\phi = 1.0\times 10^{14}$ ions/cm^2), we observe a linear dependence[41] of Δ_{1580} on the ionic mass for m in the range $9 < m < 31$ (i.e., between ^{9}Be and ^{31}P, as seen in Fig. 7). From Figs. 6 and 7 we conclude that the linewidth of the disorder-induced 1360-cm^{-1} line is more sensitive to disorder than the linewidth of the Raman-allowed 1580-cm^{-1} line.

Furthermore, from Fig. 6 we can plot the value of R_s versus implantation fluence. To find R_s, we take the skin depth of light equal to $(R_p - \Delta R_p)$ as calculated by the LSS theory for ^{27}Al ($\delta = 800$ Å), as discussed above. By considering the onset of broadening for intermediate (1.0×10^{15} ions/cm^2) and high (1.0×10^{16} ions/cm^2) fluences for ^{11}B and ^{4}He, respectively, we obtain from the relation

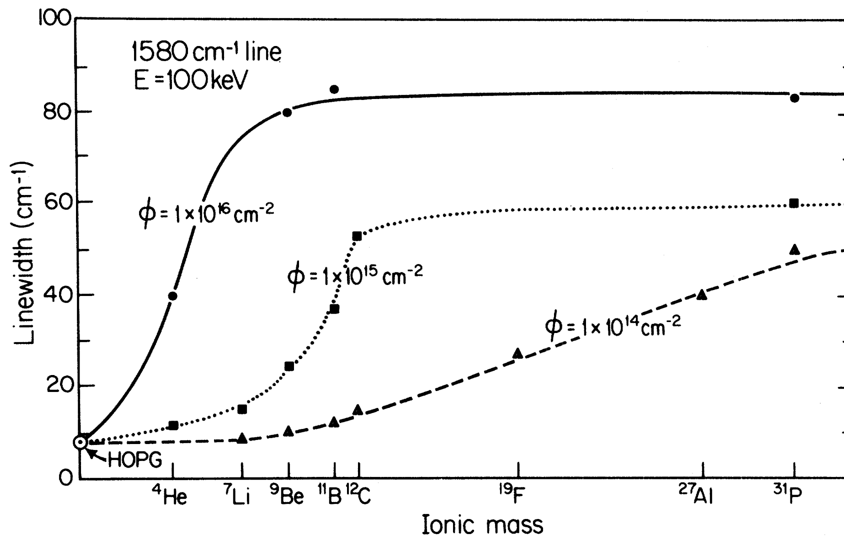

FIG. 7. Plot of the linewidth (FHWM) of the Raman-allowed 1580-cm^{-1} line vs ionic mass for HOPG implanted with 100-keV ions at different fluences.

$\delta = R_p - \Delta R_p - R_s$ the three values for R_s versus fluence given in Fig. 8. In making this plot, we note that the maximum value R_s can have for an accelerating voltage of 100 keV is the value of $R_p - \Delta R_p$ corresponding to the minimum value of m, which is for hydrogen ^{1}H ($R_s^{max} = 8423$ Å). The extrapolation of the plot in Fig. 8 is thus made to R_s^{max}, indicating that at a fluence of $\phi \sim 1 \times 10^{17}$ ions/cm^2, the lattice damage extends all the way to the surface (i.e., $R_s = R_p - \Delta R_p$) for all ions. By knowing R_p and ΔR_p for different ions implanted at $E = 100$ keV, Fig. 8 yields R_s, which can then be used to predict whether or not for 100-keV ions the highly disordered region extends to the surface of HOPG for a chosen fluence ϕ.

The crystal planar domain size L_a can be deduced from the relative intensities I_{1360}/I_{1580} shown in Fig. 9 for different ion species implanted into HOPG.[33] From our data shown in Fig. 9 it follows that the ratio of intensities I_{1360}/I_{1580} starts to saturate above a certain ionic mass, depending on the ion fluence, with the maximum value of approximately equal to 1.6, which corresponds to $L_a \sim 25$ Å. For increasing ionic mass above carbon, the increase in I_{1360}/I_{1580} is slow, independent of the parameters of implantation.

In considering the intensities of these two Raman lines, we should remember that the first-order Raman line near 1580 cm^{-1} for microcrystalline graphite is actually a doublet structure.[15,31] A closer look at the 1580-cm^{-1} structure for HOPG implanted with ^{11}B at $E = 100$ keV for different

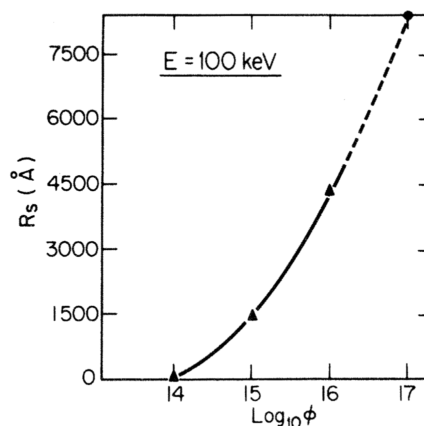

FIG. 8. Plot of R_s, the extent of the highly disordered region through which the ions have passed (see Fig. 3) vs $\log_{10}\phi$, where ϕ is the fluence of implantation of various ions into HOPG at energy $E = 100$ keV.

fluences (Fig. 10) and implanted with ^{4}He at $\phi = 1.0 \times 10^{15}$ ion/cm^2 for different ion energies (Fig. 11) shows an additional line at ~ 1622 cm^{-1} for the ^{11}B-ion-implanted samples and at 1618 cm^{-1} for the ^{4}He-ion-implanted samples. This additional line at ~ 1620 cm^{-1} corresponds to a maxima in the phonon density of states[31,32,42] and exhibits a similar behavior to the 1360-cm^{-1} disorder-induced line, as is expected from its similar origin. In this connection we note that the intensity of the 1620-cm^{-1} line increases with increasing fluence. However, the peaks at 1580 and 1620 cm^{-1} cannot be deconvolved above a fluence which corresponds to the ratio of intensities $I_{1380}/I_{1580} \sim 1.2$ and to the planar domain size

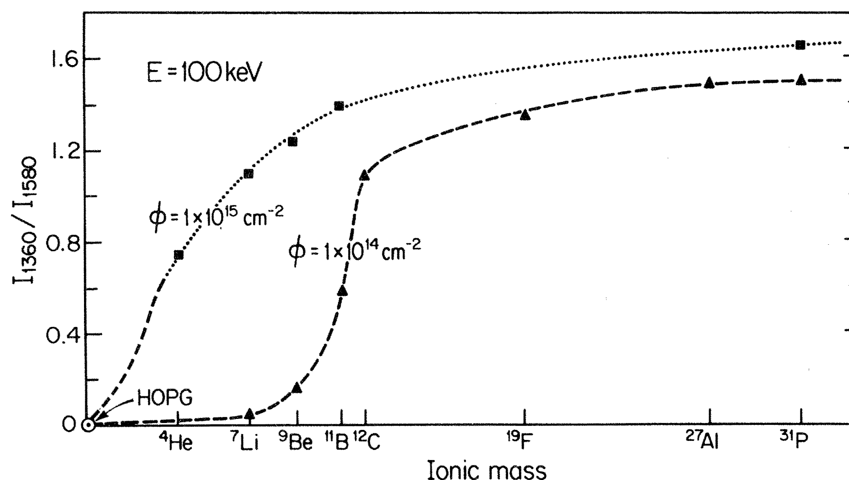

FIG. 9. Ratio of intensities of the disorder-induced ~ 1360-cm^{-1} line to the Raman-allowed ~ 1580-cm^{-1} line vs ionic mass for implantation at 100 keV for two fluences.

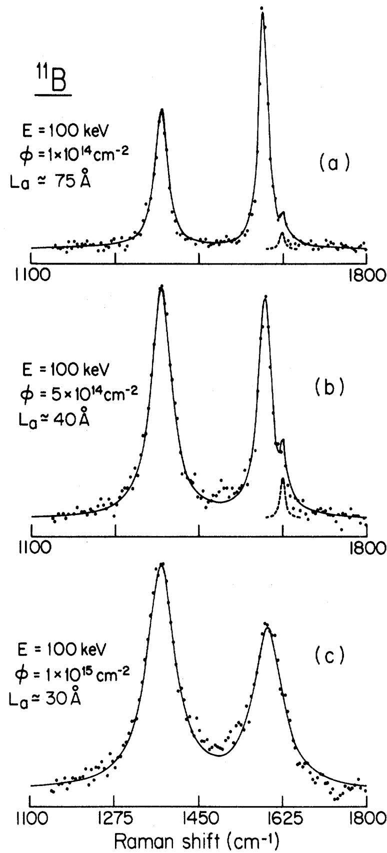

FIG. 10. First-order Raman spectra of HOPG ion-implanted with ^{11}B ($E=100$ keV) at the following fluences: (a) $\phi=1.0\times10^{14}$ ions/cm^2, (b) $\phi=5.0\times10^{14}$ ions/cm^2, and (c) $\phi=1.0\times10^{15}$ ions/cm^2. The abscissa is linear in wave number and the points are experimental. The solid curves are a Lorentzian fit to the points. The dashed curves show the fit to the disorder-induced line at ~1620 cm^{-1}. The crystalline domain size L_a deduced from each Raman spectrum is indicated (see text).

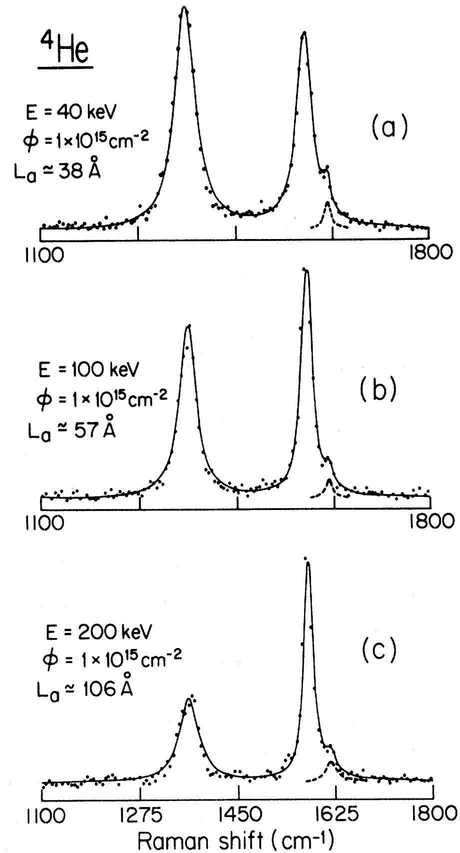

FIG. 11. First-order Raman spectra of HOPG ion-implanted with ^4He ($\phi=1.0\times10^{15}$ ions/cm^2) at the following ion energies: (a) $E=40$ keV, (b) $E=100$ keV, and (c) $E=200$ keV. The abscissa is linear in wave number and the points are experimental. The solid curves are a Lorentzian fit to the points. The dashed curves show the fit to the disorder-induced line at ~1620 cm^{-1}. The crystalline domain size L_a deduced from each Raman spectrum is indicated (see text).

$L_a\sim35$ Å. In Fig. 9, the value of $I_{1380}/I_{1580}\sim1.2$ corresponds approximately to the onset of saturation for both fluences shown in the figure.

Both the 1360- and 1620-cm^{-1} lines have counterparts in the second-order spectrum at 2735 and 3248 cm^{-1}, respectively, giving further evidence that the 1620-cm^{-1} line is also disorder-induced, as has also been suggested by Nemanich *et al.*[31] These authors also reported that they observed a significant Raman intensity in the 1100–1300 cm^{-1} region and suggested[31] that this intensity corresponds to the second-order features near 2450 cm^{-1}. We also observe an additional weak and broad feature at ~1140 cm^{-1}, which probably corresponds to the 2330-cm^{-1} line in the second-order spectrum previously reported.[5] To observe the ~1140-cm^{-1} feature, it is necessary to choose the ion species, fluence, and energy of implantation such that the intensity of the 1140-cm^{-1} feature is strong enough to be observed and the 1360-cm^{-1} line is sharp enough to be nonoverlapping with the 1140-cm^{-1} line (see Fig. 12). On this basis, we conclude that a good candidate for the observation of the ~1140-cm^{-1} feature is ^{27}Al implanted at $E=100$ keV with a fluence of $\phi=1.0\times10^{14}$ ions/cm^2 (Fig. 12). The ion-implantation study reported here suggests that the observed broad feature perhaps corresponds to the high phonon density of states near 1200 cm^{-1}.[42]

Figure 11 shows the dependence of the first-order Raman spectra on ion energy, keeping the mass and fluence parameters constant. This figure,

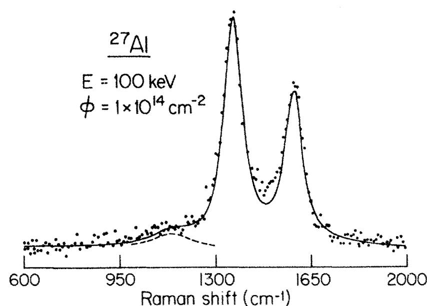

FIG. 12. First-order Raman spectrum of HOPG ion-implanted with ^{27}Al at $E=100$ keV and $\phi=1.0\times10^{14}$ ions/cm^2, providing some evidence for structure near 1140 cm^{-1} (dashed curve). The solid curve is a fit of three Lorentzian lines to the experimental points. The abscissa is linear in wave number.

plotted for ^{4}He ions at various energies, shows that, as far as the Raman spectra are concerned, decreasing the energy of implantation is qualitatively similar to increasing the fluence or ionic mass, keeping the energy constant. Decreasing the ion energy shifts the damaged region closer to the surface, matching the damaged region better to the optical skin depth. By looking at the relative intensities I_{1360}/I_{1580} of our spectra versus ion energy (Fig. 13), we see that I_{1360}/I_{1580} for the low-energy region is in good agreement with values at the onset of saturation in the curve for $\phi=1.0\times10^{15}$ ions/cm^2 in Fig. 9, and the ratio I_{1360}/I_{1580} for the high-energy limit is indistinguishable from that of pure HOPG. Thus, the sample implanted with ^{4}He at $\phi=1.0\times10^{15}$ ions/cm^2 and $E\geq300$ keV gives Raman spectra similar to HOPG, which can be understood on the basis of Fig. 13; for this energy range, the lattice damage occurs primarily beyond the optical skin depth (for ^{4}He and $E=200$ keV, we have $R_p=9415$ Å and $\Delta R_p=780$ Å).

These conclusions also follow from Fig. 14 which shows the linewidth of the 1580-cm^{-1} line versus accelerating voltage for ^{4}He ions implanted at a fluence of 1.0×10^{15} ions/cm^2. The figure shows that for energies higher than 200 keV, the linewidth of the Raman-allowed line approaches the linewidth corresponding to pristine HOPG. The effect of ionic mass must be taken into account when we compare the spectra from the samples implanted with different ions. The linewidth for the $E=40$-keV implant ($R_p=3019$ Å and $\Delta R_p=553$ Å) could be compared for example with the linewidth of HOPG implanted with ^{9}Be at the same fluence and $E=100$ keV (R_p and ΔR_p values given in Table II) which shows that $\Delta_{1580}(^9\mathrm{Be}) > \Delta_{1580}(^4\mathrm{He})$ even though $R_p(^9\mathrm{Be}) > R_p(^4\mathrm{He})$.

We now focus attention on our studies of HOPG implanted with different ions when the fluences are higher than the threshold for formation of an amorphous region extending from the surface through $[R_p+\Delta R_p]$. These phenomena are illustrated in the Raman spectra covering a wide frequency range, shown in Fig. 15(a) for ^{11}B- and Fig. 15(b) for ^{31}P-ion-implanted HOPG; all other parameters of implantation are the same. Figures 15(a) and 15(b) show the same spectra, from which we conclude that at such high fluences as 1.0×10^{16} ions/cm^2, there is no effect of ionic mass on the Raman spectra, and the entire volume between OO' and PP' in Fig. 3 is highly disordered. To fit these spectra we used in each case five broad lines, the parameters of which were determined by

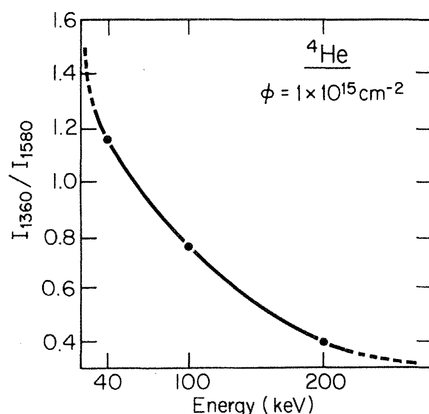

FIG. 13. Plot of the relative intensities of disorder-induced to Raman-allowed lines I_{1360}/I_{1580} vs energy of implantation for ^{4}He ions at a fluence of 1.0×10^{15} ions/cm^2.

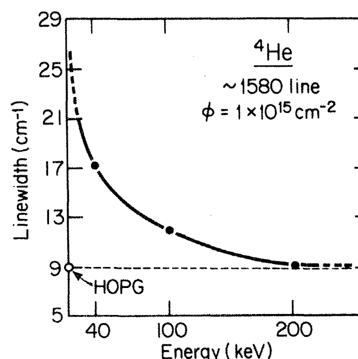

FIG. 14. Plot of the linewidth (FWHM) of the Raman-allowed line at ~1580 cm^{-1} vs energy of implantation for ^{4}He ions at a fluence of 1.0×10^{15} ions/cm^2.

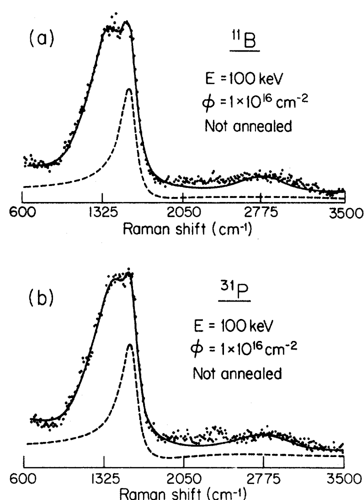

FIG. 15. Raman spectra of HOPG ion implanted at 100 keV with high fluences (1.0×10^{16} ions/cm^2) of: (a) ^{11}B ions and (b) ^{31}P ions. In each curve, the dashed curve is the contribution from the Breit-Wigner line and the solid curve is the superposition of the five Raman lines (see Table III) which provide a least-squares fit to the experimental points for the Raman spectra from the samples before annealing.

a least-squares fit and the results are presented in Table III. The broad structure peaking near 2750 cm^{-1} is identified with the second-order spectrum. All constituent lines in Table III were taken to have a Lorentzian line shape except for the Raman-allowed 1587-cm^{-1} line, which was taken to be of the Breit-Wigner type, with the coupling parameter $\Gamma/q=-20$. The dashed lines in Figs.

TABLE III. Parameters for the five lines used to fit spectra in Fig. 15. Raman spectra were taken on HOPG samples implanted with ^{11}B and ^{31}P ions at 100 keV to a fluence of 1.0×10^{16} ions/cm^2. The spectra were fitted by five Raman lines, all of which were of Lorentzian line shape, except for the line which peaks at 1587 cm^{-1} and has a Breit-Wigner line shape with $\Gamma/q=-20$.

Raman shift (cm^{-1})	Linewidth (FWHM) (cm^{-1})
700	100
1160	100
1375	180
1587	85
2750	250

15(a) and 15(b) are the Raman-allowed Breit-Wigner constituents which contribute to the spectra (solid lines). At these high fluences, the second-order graphite spectrum largely disappears and only a broad background remains, which is "peaked" at a position close to the main second-order peak of pure HOPG (2735 cm^{-1}). The Breit-Wigner line shape in high-fluence ion-implanted HOPG is found to be similar to stage-1 alkali-metal—graphite intercalation compounds.[43]

The results of our high-temperature-annealing experiments in an Ar atmosphere on HOPG ion-implanted with ^{11}B at a high fluence ($\phi=1.0\times10^{16}$ ions/cm^2 and $E=100$ keV) are related to Raman scattering results on the graphitization processes of amorphous films of carbon. Two steps of graphitization are generally considered. The first step is in-plane ordering, which occurs between 1300 and 1500 °C, and is quickly followed by the second step of graphitization above 2000 °C, where three-dimensional ordering takes place.[39] Generally x-ray diffraction experiments are performed to measure the distance d_{002}, from which it is possible to calculate the degree of graphitization.[39] Diamagnetic susceptibility measurements are also carried out to monitor the graphitization process,[39] in which saturation in χ to the HOPG value is observed for a heat-treatment temperature above 2000 °C ($\chi_s=-7\times10^{-6}$ emu). The onset of the second step of graphitization can also be determined by looking for the appearance of a shoulder in the structure near 2700 cm^{-1} in the second-order Raman spectra.[36] The Raman scattering technique is difficult to apply in this way for the characterization of the onset of the second step of graphitization because of the rapid broadening of the 2735-cm^{-1} line as defects are introduced. For most carbon blacks, the heat-treatment temperature for the onset of the second step of graphitization is found to be between 2300 and 2500 °C; for cokes it is $\sim$2000 °C.

In Fig. 16 we present the annealing-temperature dependence of the coupling parameter Γ/q of the Breit-Wigner line shape in the first-order spectrum of a sample implanted to a high fluence (1.0×10^{16} ions/cm^2). The dependence is found to be linear up to an annealing temperature of 1800 °C, and the data extrapolate to a width $\Gamma/q\to0$ at $T=2350$ °C; in analogy to the graphitization process, we identify this temperature where $\Gamma/q\to0$ with the onset of three-dimensional ordering. We therefore conclude that the measurement of the Γ/q parameter provides a technique for the characterization of

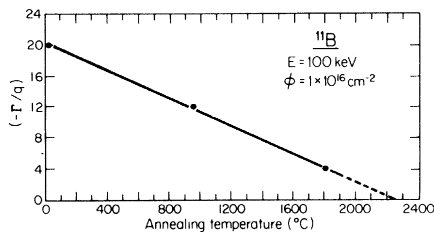

FIG. 16. Dependence on annealing temperature of the coupling parameter Γ/q of the Breit-Wigner line in the first-order spectra for ^{11}B ions implanted at 100 keV at a fluence of 1.0×10^{16} ions/cm^2.

three-dimensional ordering during the annealing process of ion-implanted graphite samples.

Above the temperature where the coupling parameter (Γ/q) vanishes, the graphitization process still can be followed with Raman spectroscopy by looking at (1) the intensity of the disorder-induced line at ~ 1360 cm^{-1}, which does not exist in pure HOPG, (2) the linewidth of the ~ 1580-cm^{-1} line in the first-order spectra, and (3) the line shape and linewidth of the ~ 2735-cm^{-1} line in the second-order spectra, which is a doublet in pure HOPG. The completion of the graphitization process is reached when all of these parameters of the spectra from annealed samples are indistinguishable from those of HOPG. The annealing temperature for full graphitization strongly depends on whether or not the highly disordered region extends all the way to the surface of the ion-implanted samples. That is, when $R_s \approx R_p - \Delta R_p$, the temperature for complete graphitization is considerably higher than for smaller values of R_s. This result is similar to that observed in the annealing of ion-induced lattice damage in semiconductors.[1]

IV. SUMMARY

It is shown in this work that the lattice damage caused by implanting ions into graphite can be characterized by several complementary techniques, with Raman scattering as the dominant technique. All characterization results presented here are interpreted in terms of a highly damaged region through which the ions pass (characterized by R_s) prior to coming to rest between $R_p - \Delta R_p$ and $R_p + \Delta R_p$.

The implantation parameters used to interpret the Raman spectra, R_p and ΔR_p, are determined using the LSS theory.[7] Depth-profile studies using AES have been carried out to verify the validity of this theory (originally derived for noncrystalline materials) for the implantation into *c* faces of HOPG.

Keeping the laser frequency constant (and hence also the optical skin depth), the distance of the implantation region from the surface has been varied. The onset of a rapid increase in linewidth for the disorder-induced 1360-cm^{-1} Raman line corresponds to the matching of the optical skin depth δ to the region of extensive lattice damage (between MM' and PP' in Fig. 3). From analysis of these linewidth versus ionic mass curves, the dependence of R_s on ion fluence is deduced. These measurements of R_s are closely correlated with the SEM measurements, which show a significant increase in surface damage as $R_s \rightarrow R_p - \Delta R_p$.

From the magnitude of the relative intensities I_{1360}/I_{1580}, the size of the ordered crystallite domains L_a can be determined and good agreement is obtained with measurements of these domain sizes by electron micrographs taken with the STEM. The intensity of the disorder-induced Raman line near 1620 cm^{-1}, also corresponding to a peak on the density of states, can be used to monitor the lattice damage in some cases.

Several other aspects of the Raman spectra of ion-implanted graphite are investigated, including (1) the dependence of the disorder-induced 1360-cm^{-1} line and the Raman-allowed line at 1580 cm^{-1} on ion energy, and (2) the line shape at high ion fluences of the Raman-allowed line near 1580 cm^{-1} and of the second-order spectrum. Analysis of the Breit-Wigner line shape of the Raman-allowed line as a function of annealing temperature shows that the magnitude of the Breit-Wigner coupling parameter can be correlated with the graphitization of the damaged region as the lattice damage is annealed out. We also note similarities in line shape between both the Breit-Wigner Raman-allowed line and the second-order Raman spectra of ion-implanted graphite and of intercalated stage-1 alkali-metal compounds.

ACKNOWLEDGMENTS

We wish to thank M. Rothman and Dr. J. P. Donnelly (MIT Lincoln Lab) for assistance with the ion implantation, J. Martin for assistance with the Auger measurements, Dr. A. J. Garratt-Reed for assistance with the STEM measurements, Dr.

A. Moore of the Union Carbide Corporation for the generous donation of the HOPG material, and Dr. E. W. Maby for helpful discussions. We also gratefully acknowledge ONR Grant No. N00014-77-C-0053 for support of this research and gratefully acknowledge use of the ion-implantation, SEM, STEM, and Surface Analytical Central Facilities of the Center for Materials Science and Engineering. The Francis Bitter National Magnet Laboratory is supported by the National Science Foundation (NSF).

---

*Now at ARCO Chemical Co., 3801 Westchester Pike, Newtown Sq., PA 19073.

[1]J. W. Mayer, L. Eriksson, and J. A. Davis, *Ion Implantation in Semiconductors* (Academic, New York, 1970).

[2]B. L. Crowder, in *Ion Implantation in Semiconductors,* edited by S. Namba (Plenum, New York, 1972), p. 63.

[3]B. L. Crowder, J. E. Smith, Jr., M. H. Brodsky, and M. I. Nathan, in *Proceedings of the Second International Conference on Ion Implantation in Semiconductors, Garmisch-Partenkirchen, 1970,* edited by I. Ruge and J. Grant (Springer, Berlin, 1971), p. 255.

[4]J. E. Smith, Jr., M. H. Brodsky, B. L. Crowder, and M. I. Nathan, J. Non-Cryst. Solids 8-10, 179 (1972).

[5]B. S. Elman, M. S. Dresselhaus, G. Dresselhaus, E. W. Maby, and H. Mazurek, Phys. Rev. B 24, 1027 (1981).

[6]M. S. Dresselhaus and G. Dresselhaus, Adv. Phys. 30, 139 (1981).

[7]J. Lindhard, M. Scharff, and H. E. Schiott, Dan. Vidensk. Selsk., Mat. Fys. Medd. 33, 14 (1963).

[8]L. C. Northcliffe and R. F. Schilling, Nucl. Sect. A 7, 233 (1970).

[9]G. Dearnaley, J. H. Freeman, G. A. Gard, and M. A. Wilkins, Can. J. Phys. 46, 587 (1968).

[10]R. Beserman and T. Bernstein, J. Appl. Phys. 48, 1548 (1977).

[11]H. Engstrom and J. B. Bates, J. Appl. Phys. 50, 2921 (1979).

[12]G. Lucovsky, in *Proceedings of the Fifth International Conference on Amorphous and Liquid Semiconductors, Garmisch-Partenkirchen, 1973,* edited by J. Stuke and W. Brenig (Taylor and Francis, London, 1974), p. 1099.

[13]M. I. Nathan, J. E. Smith, Jr. and K. N. Tu, J. Appl. Phys. 45, 2370 (1974).

[14]R. B. Wright, R. Varma and D. M. Gruen, J. Nucl. Mater. 63, 415 (1976).

[15]H. Maeta and Y. Sato, Solid State Commun. 23, 23 (1977).

[16]J. F. Morhange, G. Kanellis, M. Balkanski, J. F. Peray, J. Icole, and M. Croset, in *Proceedings of the Symposium on Laser-Solid Interactions and Laser Processing,* edited by S. D. Ferris, H. J. Leamy, and J. M. Poate (AIP, New York, 1979), p. 429.

[17]J. F. Morhange, G. Kannellis, and M. Balkanski, Solid State Commun. 31, 85 (1979).

[18]T. Kamiya, M. Kishi, A. Ushirokawa, and T. Katoda, Appl. Phys. Lett. 38, 377 (1981).

[19]E. C. Baranova, V. M. Gusev, Yu. V. Martynenko, C. V. Starinin, and I. B. Haibullin, Radiat. Eff. 18, 21 (1973).

[20]B. L. Crowder, R. S. Title, M. H. Brodsky, and G. D. Pettit, Appl. Phys. Lett. 16, 205 (1970).

[21]J. C. Bourgoin, J. F. Morhange, and R. Beserman, Radiat. Eff. 22, 205 (1974).

[22]A. Mooradian and G. B. Wright, Phys. Rev. Lett. 16, 999 (1966).

[23]M. Balkanski and W. J. Nazarewicz, J. Phys. Chem. Solids 25, 474 (1964); 27, 671 (1966).

[24]R. Beserman, M. Jouanne, and M. Balkanski, in *Proceedings of the Eleventh International Conference on the Physics of Semiconductors, Warsaw, 1972* (PWN—Polish Scientific Publishers, Warsaw, 1972), p. 1181.

[25]F. Cerdeira, T. A. Fjeldly, and M. Cardona, Phys. Rev. B 9, 4344 (1974).

[26]R. S. Krishnan, Proc. Indian Acad. Sci. 24, 25 (1946).

[27]M. H. Cohen and J. Ruvalds, Phys. Rev. Lett. 23, 1378 (1969).

[28]S. A. Solin and A. K. Ramdas, Phys. Rev. B 1, 1687 (1970).

[29]R. J. Nemanich, G. Lucovsky, and S. A. Solin, in *Proceedings of the International Conference on Lattice Dynamics, Paris, 1974,* edited by M. Balkanski (Flammarion, Paris, 1975), p. 619.

[30]M. Nakamizo, R. Kammereck, and P. Walker, Jr., Carbon 12, 259 (1974).

[31]R. J. Nemanich and S. A. Solin, Phys. Rev. B 20, 392 (1979).

[32]R. J. Nemanich, G. Lucovsky, and S. A. Solin, Mater. Sci. Eng. 31, 157 (1977).

[33]F. Tuinstra and J. L. Koenig, J. Chem. Phys. 53, 1126 (1970).

[34]P. C. Eklund, D. S. Smith, V. R. K. Murthy, and S. Y. Leung, Synthetic Metals 2, 99 (1980).

[35]S. A. Solin and R. J. Kobliska, in *Proceedings of the Fifth International Conference on Amorphous and Liquid Semiconductors, Garmisch-Partenkirchen, 1973,* edited by J. Stuke and W. Brenig (Taylor and Francis, London, 1974), p. 1251.

[36]A. Marchand, P. Lespade (private communication); A. Marchand, P. Lespade, and M. Covzi, *Extended Abstracts of the Fifteenth Biennial Conference on Carbon, University of Pennsylvania, 1981,* edited by W. C. Forsman (University of Pennsylvania Press, Philadelphia, 1981), p. 282.

[37]N. Wada, P. J. Gaczi, and S. A. Solin, J. Non-Cryst. Solids 35/36, 543 (1980).

[38]M. S. Dresselhaus and G. Dresselhaus, in *Topics in Applied Physics,* edited by M. Cardona and G. Günderodt (Springer, Berlin, 1982), Vol. 51, Chap. 2.

[39]A. Marchand and A. Pacault, *Nouveau Traite De Chemie Minerale,* edited by P. V. H. Pascal (Masson, Paris, 1968), Vol. VIII, No. 1, p. 457.

[40]J. D. Jackson, *Classical Electrodynamics* (Wiley, New York, 1966), p. 225.

[41]B. S. Elman, G. Dresselhaus, and M. Shayegan, in *Extended Abstracts of the Fifteenth Biennial Conference on Carbon, University of Pennsylvania, 1981,* edited by W. C. Forsman (University of Pennsylvania Press, Philadelphia, 1981), p. 24.

[42]R. Al-Jishi, B. S. Elman, and G. Dresselhaus, in *Extended Abstracts of the Fifteenth Biennial Conference on Carbon, University of Pennsylvania, 1981,* edited by W. C. Forsman (University of Pennsylvania Press, Philadelphia, 1981), p. 34.

[43]P. C. Eklund and K. R. Subbaswamy, Phys. Rev. B 20, 5157 (1979).

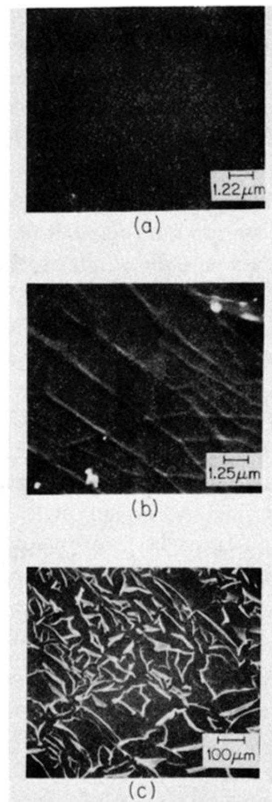

FIG. 4. (a) Scanning electron micrograph of pristine HOPG showing a smooth structureless surface. (b) Scanning electron micrograph of the ^{75}As-ion-implanted sample. The fluence was 1.0×10^{15} ions/cm^2 at 100 keV. (c) Scanning electron micrograph of the ^{31}P-ion-implanted sample. The fluence was 1.0×10^{17} ions/cm^2 at 100 keV. The micrograph shows extensive surface damage for implantation at this high fluence.

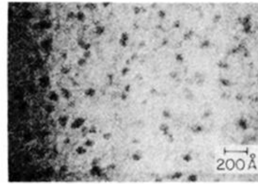

FIG. 5. STEM bright-field micrograph taken on a ^{75}As-ion-implanted sample with a fluence of 1.0×10^{15} ions/cm^2 at 100 keV. The dark areas correspond to crystalline regions (see text).